NJC

PAPER

Check for updates

Nickel and cobalt transfigured natural clay: a green catalyst for low-temperature catalytic soot oxidation†

Devika Laishram, R. Krishnapriya, [ID] Bhagirath Saini, Unnati Gupta, Vineet K. Soni and Rakesh K. Sharma [ID] *

Soot particulates in engine exhausts pose a severe threat to the environment and human health – causing cancer, affecting the heart and lungs and drives metal processes. This study proposes a practical, real-world application of transition metal modified natural clay as an environmentally benign, low-cost, green catalyst for soot oxidation. Ni and Co (NC-Clay) incorporated natural clay catalysts were prepared by a simple wet impregnation method and meticulously characterized by different characterization techniques. The catalyst exhibited higher H_2 absorption at a lower temperature with similar trends as observed in O_2 TPD that indicated a remarkable redox property, which is useful for applications as a catalyst in soot oxidation. Excellent catalytic activity with a very low T_{50} of 358 °C was observed and can be accredited to the improved surface oxygen vacancies and thermal stability by the metal modification of clay.

Introduction

The World Health Organisation in 2012 estimated 6.5 million deaths due to outdoor and indoor air pollution, which accounts for 11.6% of all global deaths. Furthermore, 90% of them occur in low- and middle-income countries, especially in South East Asia and Western Pacific regions. Major diseases related include cardiovascular, pulmonary, and lung cancer.[1] Of the various pollutants, particle pollution of soot is considered one of the lethal forms of air pollution. Soot, as defined by the Oxford Dictionary, is a "deep black powdery substance consisting of largely amorphous carbon produced by incomplete burning of organic matter."[2] Alternately, soot is a particle pollutant having 2.5 μm or smaller diameter (2.5 PM or 2.5 particulate matter) causing tremendous hazards to health and the environment.[3] Soot pollution is catastrophic since the particulate matter is so small that it can be transferred from the mother to the unborn child through the bloodstream's placenta.[4]

One of the effective methods used to curb soot pollution is using diesel particulate filters in exhaust engines. However, the commercially available filters that use Pt catalysts in their design are costly. Also, the poisoning of Pt occurs very readily;

hence, economically viable catalysts have been promoted to replace Pt. Consequently, as an alternative to Pt catalyst for soot oxidation, various materials have been reported, such as ceria, hafnia, zirconia, transition metal catalysts based on Co, Cu, Fe, and Mn – doping on ceria, and composition of ceria with Pr, La, *etc.*,[5–14] which are summarized in Table S1 (ESI†). Apart from these, transition metals, rare earth oxides, and mixed oxides such as CeO_2, SiO_2, and Al_2O_3 have been explored to boost soot oxidation activity.[15] Additionally, composites of noble metals with CeO_2 have been used for soot oxidation, such as Pt, Pd, Ru, and Rh.[16–19] However, all these catalysts work at high temperatures (>400 °C), and therefore it is imperative to develop efficient and affordable catalysts desirably with low oxidation temperature. CeO_2 is considered suitable as it has good redox activity between Ce^{4+} and Ce^{3+}, showing adequate oxygen storage capacity. The T_{50} temperature, which is the temperature at which 50% of the total weight loss occurs, is lowered when the active species such as oxides and superoxides spill over the surface of the soot.

Makkee *et al.* observed redox activity in the process of catalytic oxidation of soot using CeO_2 while performing a transient kinetic experiment with labelled oxygen.[20] Additionally, they also proposed that there is the creation of vacant sites due to CeO_2 reduction during the process. For metal doping such as Ag/CeO_2, Shimizu *et al.* proposed that initially, O_2 gets chemisorbed on sites where oxygen vacancies are located near the nanoparticle catalyst such as Ce^{3+} and Ag.[21] This process gives rise to reactive oxygen species such as oxides and superoxides with high

Sustainable Materials and Catalysis Research Laboratory (SMCRL), Department of Chemistry, Indian Institute of Technology, Jodhpur NH 65, Karwar, Jodhpur-342037, India. E-mail: rks@iitj.ac.in
† Electronic supplementary information (ESI) available. See DOI: 10.1039/d1nj01346g

reducibility that migrate towards the soot surface to oxidize the C into CO_2. This also leads to creating more oxygen vacant sites and oxidized nanoparticles such as Ce^{3+} at the interface with the catalyst. Additionally, Zhao *et al.* suggested two pathways with which catalyst-based soot combustion occurs in the presence of NO_x/O_2. The first is the combustion of soot directly into CO_2 *via* the active oxygen species present on the surface. The second is the combustion using NO and O adsorbed species, which are activated into active NO^+ and O^- species by the metal nanoparticle catalyst. The resultant active species react at the interface between the metal oxide catalyst to form NO_2, which is a more potent oxidant and reduces to NO by the carbon present as soot.[22]

Some critical parameters that are substantial for excellent soot oxidation activity of catalysts include the number of active components, chemical attributes, and the catalyst–support interaction. The cumulative effect of these properties governs the outstanding catalytic efficiency towards soot oxidation. Among the various metal species, oxides of cobalt emerge as the potential catalyst for combustion reactions due to their amenability to release lattice oxygen at low temperatures.[23] Successively, many binary oxides of cobalt with others such as CeO_2, K, Mn, Pd, Cu, K, *etc.* have been reported. Additionally, metal-based catalysts such as $CoAl_2O_4$, $Ni/CoAl_2O_4$, and Pt, $Ni/CoAl_2O_4$ have been explored with the objective of reducing Pt content in the catalyst used for soot oxidation.[24] These catalysts were capable of modifying the electronic structure and shifting the d-band, thereby promoting vacant oxygen sites for better soot oxidation activity.[25] Moreover, catalytic soot oxidation is mechanistically a gas–solid–solid interfacial reaction governed by the contact between the catalyst and the soot particles. In this regard, the incorporation of nanoparticles (NPs) into a suitable support system can maximize the surface area with a better interconnection between the catalyst and soot, which significantly improves the overall efficiency.[26] In our earlier studies, we have demonstrated the successful implementation of clay-supported metal catalysts for biomass conversion.[27,28] Clay has inherent properties such as large surface areas, broken edge bonds, and ion exchange which increases the adsorption, absorption, and catalytic properties. Additionally, clay interlayers are in the nanometre range that can be tuned and engineered to highly active green catalysts.[29,30]

To explore further, we propose Ni and Co modified clay as a propitious catalyst support for the soot oxidation application. The bimetals are expected to enhance the catalytic property of the system by a compound effect of improvement in terms of redox property, textural improvement, increasing active sites, and augmenting surface oxygen vacant sites. This work reports for the first time an investigation of the effect of incorporating bimetals Ni and Co on clay substrates pertaining to soot oxidation application.

Experimental section

Natural clay was obtained from Barmer in Rajasthan, India, which is composed of montmorillonite. Nickel nitrate hexahydrate and

Co nitrate hexahydrate precursors were purchased from Alfa Aesar.

Methods

The preparation of the catalyst was similar to the one prepared earlier in our study.[27] Briefly, natural clay was processed thoroughly three times using DI water to remove any impurities present *via* sedimentation. The obtained clay was stirred vigorously and then kept undisturbed to settle down, followed by drying in an oven at 120 °C. A 4% salt of Ni precursor was dissolved in 4 N HNO_3 and stirred until it became a paste. After the paste has dried, the catalyst prepared was ground and calcined at 500 °C under an N_2 atmosphere. To make a bi-metal alloy doped clay catalyst a similar procedure was adopted for doping with Co. Lastly, the Ni and Co-doped clay was calcined under a H_2 atmosphere. Briefly, 198 mg $Ni(NO_3)_2$ and 395 mg $Co(NO_3)_2$ were mixed thoroughly with 1 g of the processed clay, and 10 mL of 3 N nitric acid was added. The mixture was stirred well to form a uniform paste. A ratio of $1:2$ of Ni and Co was maintained during this process. The paste thus obtained was dried and ground in a mortar pestle before annealing in a tubular furnace.

Catalyst-soot preparation

Soot used for the laboratory testing was Printex-U procured from Degussa. The prepared catalysts and the soot were ground in a mortar pestle to obtain tight contact between the soot and catalyst. The catalyst and soot were taken in a $4:1$ ratio and ground for a period of 15 minutes before subjecting to analysis.

Characterization

H_2 Temperature Programmed Reduction (TPR) and O_2 Temperature Programmed Desorption (TPD) were performed with the help of a Chemisorption Analyzer (AMI-300) from Altamira Instruments, USA. The O_2 TPD measurement was preceded by a pre-treatment in He at a temperature of 500 °C for 1 h, followed by purging with He for 2 h to ensure the removal of any adsorbed species. The O_2 TPD measurement was performed with a heating rate of 10 °C min^{-1} at temperatures ranging from 100 °C to 1000 °C. For the TPR measurements, the sample under consideration was subjected to pre-treatment at a rate of 10 °C min^{-1} for 1 h under helium until a temperature of 150 °C and then cooled afterward to ambient temperature. For reduction, a mixture of H_2 and He (5:95) flowed at a rate of 30 mL min^{-1}, and measurements were taken from 30 °C to 900 °C. XRD measurements were performed using a Bruker D8 Advance diffractometer equipped with Cu Kα as the radiation source. An Autosorb IQ-MP-XR of Quantachrome Instruments, USA, was used for adsorption–desorption measurements to perform surface area analysis. Thermogravimetric (TGA) measurements were performed in an STA (Simultaneous Thermal Analyser) – 6000 from PerkinElmer. To study the morphological and elemental composition, an FEI Tecnai-G2 T20 Transmission Electron Microscope (TEM) was used. FTIR was performed using an FTIR spectrometer from Bruker Vertex

(70 V, PMA50) within the range from 400 cm^{-1} to 4000 cm^{-1} at room temperature.

Results and discussion

Natural clay was procured from Barmer in Rajasthan, India, mainly comprising montmorillonite[31] and was impregnated with Ni and Co metals after washing thoroughly. The detailed process is pictorially represented in Scheme 1. Briefly, the locally procured clay was washed thoroughly three times, followed by letting the clay settle. The obtained clay is dried overnight at 120 °C and then ground into a fine powder. Precursors of Ni and Co, namely, $Ni(NO_3)_2$ and $Co(NO_3)_2$ are stirred in a 10 mL 3 N HNO_3 solution after which 1 g clay is added and stirred to make the solution homogenous. As the solution becomes more viscous, the stirring is stopped with continued heating for 3 h. After grinding finely, the material is calcined under a N_2 atmosphere at 500 °C for 5 h followed by annealing under H_2 for 3 h at 300 °C. The synthesized NC-Clay catalyst is analysed through various characterization techniques. Additionally, catalytic activity studies using TGA with O_2 TPD and H_2 TPR using zero air (a mixture of oxygen and nitrogen with fewer hydrocarbons) were performed. The further experimental procedure is given in the ESI.†

The morphological characterization of the prepared NC-Clay catalyst is illustrated by the TEM image in Fig. 1, showing the size, and crystallinity. The images in Fig. 1a–c show the interlayers of clay with a spacing of about an average of approximately 6 nm. The HRTEM image in Fig. 1d was analysed using Gatan DigitalMicrograph to calculate the d spacing value. The d-spacing of 0.45 nm and 0.44 nm, as indicated, corresponds to a peak at 19.5 2θ degrees as indicated in the XRD pattern in Fig. 2a. The FFT of planes in a different direction in this region is indicated in Fig. S1 (ESI†) with the corresponding IFFT. The SAED pattern of the NC-catalyst in Fig. 1e showed bright spots, indicating polycrystalline nature of the synthesized catalyst, with the innermost circle corresponding to that of the lattice spacing observed in the HRTEM image in Fig. 1d. The XRD pattern of the catalysts is shown in Fig. 2a and b, which revealed the presence of both montmorillonite and quartz with the highest intense peak at 26.5° for quartz. It indicates that the laminar stack of the doped clay is
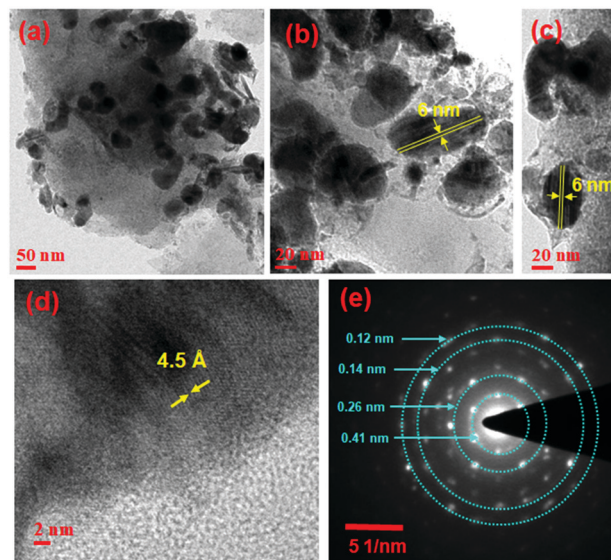

Fig. 1 (a–c) TEM images at different scales, (d) HRTEM image, and (e) SAED of the NC-Clay catalyst.
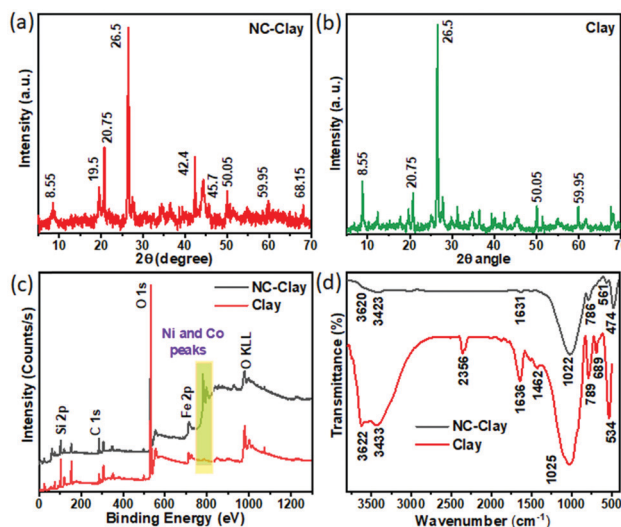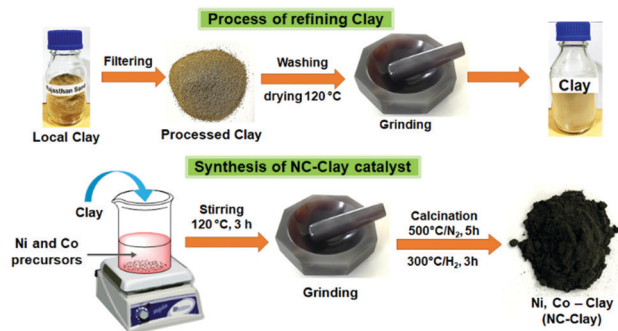

Fig. 2 (a) and (b) XRD pattern, (c) XPS survey scans, and (d) FTIR spectra of the synthesized clay and NC-Clay catalyst.

Scheme 1 Schematic representation of clay processing and catalyst preparation.

intact with proper orientation after subsequent doping with metal NPs similar to undoped clay. As a minimal weight percentage of Ni and Co was used for doping, XRD reflections from these metals are found to overlap with the clay patterns. Fig. 2c presents the XPS survey scan of the NC-Clay and clay. The highlight shows Ni and Co peaks in the NC-Clay catalyst in comparison to clay where no such peaks were observed, which confirm the presence of both the metals in the catalyst system. The IR spectrum of the as-synthesized clay and doped NC-Clay is given in Fig. 2d. The broad peaks at around 3620 cm^{-1} and 3423 cm^{-1} characterize the presence of structural –OH group and –OH stretching of the water molecule adsorbed on the NC-Clay. The peak at around 1631 cm^{-1} can be attributed to the bending of the –OH group of

the adsorbed water molecules. Broadly, quartz is identified by the presence of bands in the wavenumber region from 1200 to 500 cm^{-1}. The peaks at around 786 cm^{-1} (and the extra peak at 689 for the as-synthesized clay) and 1022 cm^{-1} can be attributed to the deformation of the Si–O–Si bond, whereas the peaks at 561 cm^{-1} (in NC-Clay) and 534 cm^{-1} (in clay) can be ascribed to the Si–O–Al bond in the materials. The peak at 2356 cm^{-1} can be assigned to atmospheric CO_2 and is observed only in the Clay catalyst and absent in the NC-Clay catalyst.

To analyze the surface properties, such as pore size and surface area of the catalyst, the BET N_2 adsorption–desorption measurement was undertaken as shown in Fig. 3. The type of behavior shown by the clay (Fig. 3a) and NC-Clay sample (Fig. 3b) is type II isotherm, which is a characteristic feature of macroporous and non-porous materials. Here, monolayer formation is followed by multilayer adsorption on the surface of the sample, resulting in unrestricted multilayer formation. As can be seen, there is an inflection point at about 0.5 relative pressure, which is an indication of the start of multilayer formation and can be called the knee point. This is representative of nanoparticles forming plate-like aggregates and unfilled macropores. The plate-like aggregation often leads to the formation of slit-shaped pores. The surface area of the NC-Clay was found to be 46 m^2 g^{-1} which is almost equivalent to that of clay (44 m^2 g^{-1}). The pore size distribution shows similar distribution as shown in Fig. 3c and d. The slight decrease in the specific area in NC-Clay compared to Ni-Clay and Co-Clay might be due to particle agglomeration as a result of the incorporation of both Ni and Co simultaneously (refer to Table 1).

The high-resolution XPS spectra of Co 2p (Fig. 4a) show $2p_{1/2}$ and $2p_{3/2}$ spin–orbit splitting. The shake-up satellite peaks corresponding to these two peaks are approximately at a distance of 6 eV from the main peak, which is a characteristic of Co_3O_4.[32] The high-intensity Co $2p_{3/2}$ peak at 780.58 eV is deconvoluted using a Gaussian–Lorentzian function and is fitted to two peaks at 780.08 eV and 782.58 eV. The two satellite peaks at 787.08 eV and 803.58 eV can be assigned to the occurrence of multiple electron excitation from Co^{2+} and Co^{3+}.[33] This might be an indication of the presence of both divalent oxides and hydroxides in the catalyst.[34]

The Ni 2p (Fig. 4b) can be deconvoluted into two spin–orbit doublets at 856.1 eV and 873.5 eV with peaks at 861.8 eV and 881.46 eV assigned to satellite peaks of Ni $2p_{3/2}$ and Ni $2p_{1/2}$, which is a typical characteristic of the Ni^{2+} peak.[35,36] This indicates the presence of active Ni and Co species with 3.23 at% and 6.54 at% as detected by the XPS in the NC-Clay catalyst (maintaining a Ni : Co ratio of 1 : 2 similar to the synthesis process) that helps in soot oxidation.

The C 1s of the NC-Clay catalyst compared to clay (Fig. S2a and b, ESI†) shows a broad peak which is deconvoluted to three smaller peaks at 284.8 eV, 286.4 eV, and 288.69 eV corresponding to C–C, C–O–C, and O–C=O, respectively. The peaks at 293.6 eV and 296.38 eV can be related to weaker peaks of K $2p_{3/2}$ and K $2p_{1/2}$, which overlap with the C 1s. The high-resolution O 1s XPS spectra of NC-Clay (Fig. 4d) are deconvoluted into two peaks at 529.7 eV and 531.6 eV. The former can be assigned to the presence of O^{2-} ions. In contrast, the latter is a characteristic of weakly adsorbed species and coordination of oxygen species in the subsurface, which indicates the presence of defective metal oxides of Ni and Co.[37] The oxygen species at lower binding energy can be assigned to the lattice oxygen (O_{latt}). The oxygen species at higher binding energy can be representative of surface adsorbed oxygen (O_{surf}). It can be observed that the oxygen at lower binding energy is not present in the clay catalyst (Fig. 4c) compared to the NC-Clay catalyst that showed the presence of lattice oxygen present at a lower binding energy of 529.5 eV (Fig. 4d).

The absence of lattice oxygen in the uncatalyzed clay indicates the absence of any labile oxygen to participate in the soot oxidation reaction.[6] Another element that promotes soot oxidation by lowering the temperature is K. However, the K used is in higher percentages; for example, Miro *et al.* used 4.5% by weight as a support on MgO/CeO_2.[38] The K present in the present study as can be observed from the XPS study (in the ESI,† Fig. S2c and d) is a composition of the catalysts which amounts to only 0.74 at% and 0.57 at% in pristine clay and NC-Clay respectively. Therefore, the effect of K to release the oxidized gases such as CO_2 through intermediate species would be negligible. In addition to the XPS spectra, the O_2 TPD profiles of NC-Clay and pristine clay catalysts (Fig. 5a and b) account for the interaction of the catalyst with various oxygen species. Oxygen species can be assigned to four different entities – O_α ($O_{2(ads)}$), O_β ($O^-_{(ads)}$), O_γ ($O^-_{(ads)}$) and O_δ ($O_2^{2-}_{(ads)}$) according to the temperatures at which they get desorbed.[39] The initial desorption for the NC-Clay catalyst might indicate the presence of physisorbed oxygen species on the surface at 240 °C, which are absent in the clay catalyst.[40] This demonstrates that incorporating Ni and Co into the NC-Clay catalyst has led to the desorption of $O\alpha$. Similar trends can be observed in the chemical analysis using XPS, where the lattice oxygen is absent in the clay catalyst. Both the catalysts showed the
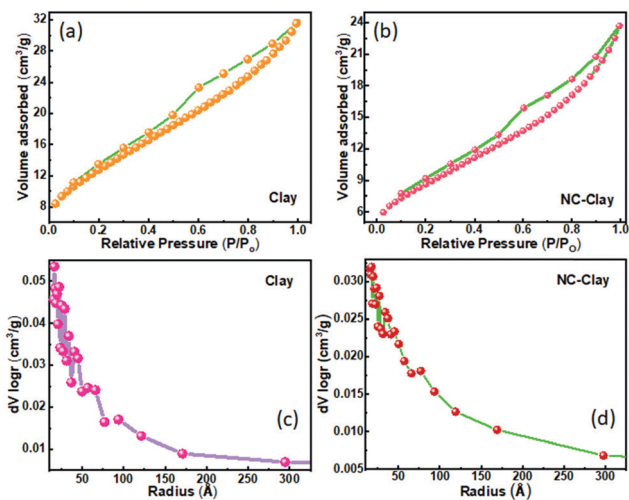

Fig. 3 (a) and (b) Present the N_2 adsorption–desorption BET isotherm of clay and NC-Clay respectively, and (c) and (d) pore size distribution of the synthesized clay and NC-Clay catalyst.

Table 1 Properties of the catalyst from BET, XPS, and H_2 TPD

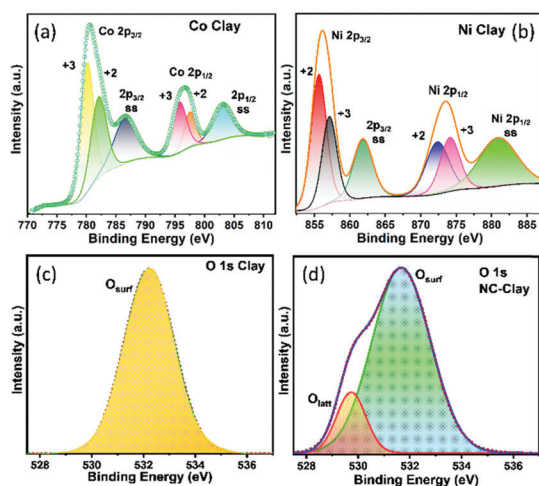| Sl. No. | Catalyst | Pore size (nm) | BET surface area ($m^2\ g^{-1}$) | O 1s peak deconvolution | | H_2 TPR temperature (°C) | H_2 consumption ($\mu mol\ g^{-1}$) | T_m soot-oxidation (°C) |
				O_{surf} peak	O_{latt} peak			
1	Clay	236	44	532.2	—	553	219	566
						795	120	
2	NC-Clay	231	46	531.7	529.7	262	1103	358
						470	1688	
3	Ni clay	232	51	—	—	532	171	566
						607	1451	
4	Co clay	230	51	—	—	354	169	538
						425	1389	

Fig. 4 High-resolution XPS (a) Co 2p and (b) Ni 2p scan of the NC-Clay catalyst, and (c) O 1s spectra of clay and (d) NC-Clay catalyst.
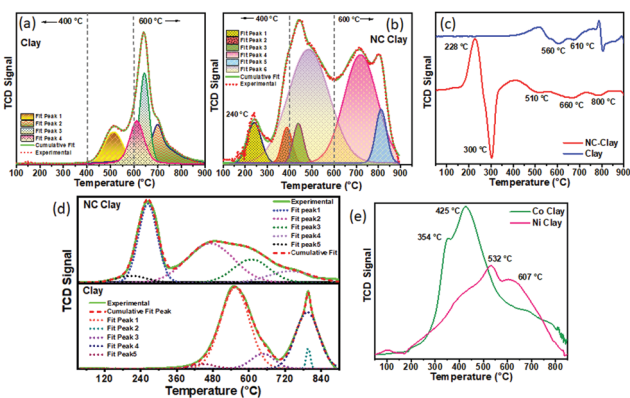
Fig. 5 High-resolution O_2 TPD of (a) clay and (b) NC-Clay catalyst with their corresponding deconvoluted profile, and 1st order derivative (c) and deconvoluted H_2 TPR thermograms of (d) Clay and NC-Clay and (e) Ni Clay and Co Clay catalysts.

presence of O_β ($O^{2-}_{(ads)}$) and O_γ ($O^{-}_{(ads)}$) in a temperature range between 400 °C and 600 °C, which can be attributed to subsurface movement of O^-.[41] The desorption of O_β and O_γ shows the reducibility of the metal atoms present, which generates oxygen vacancies in the catalyst.[42] The oxygen species desorbed at a higher temperature beyond 600 °C correspond to

the oxygen incorporated into the crystal structure. It can be observed that the incorporation of Ni and Co into the NC-Clay catalyst has significantly altered the oxygen desorption in the solid. This can be because incorporating new materials leads to the formation of boundaries and interfaces. Such events will significantly enhance the diffusion of subsurface and bulk oxygen species towards the surface, thereby altering the valency of the lattice constituents and thus changing the redox property of the catalyst.[43] Additionally, peaks observed at a lower temperature in the NC-Clay indicate the presence of labile oxygen species capable of participating in redox activity. The observed desorption of the NC-Clay catalyst showed more substantial desorption capacity compared to clay which confirms the improved mobility of lattice oxygen in the former.[44] The synergy of simultaneous incorporation of Ni and Co creates vacant oxygen sites and promotes active surface adsorbed oxygen species. Moreover, the hydrogen annealing is bound to create additional defect sites and defect species, inducing more labile and surface-active oxygen species, which is in agreement with XPS and O_2-TPD.

The H_2 TPR studies show two main zones of reduction – one at a lower temperature (below 600 °C) and the other at a higher temperature (above 600 °C). Fig. 5c shows the first-order derivative of the thermograms, which enables the study of the reducibility of the catalyst. The one-step reduction can be accounted as the primary reduction peak at around 300 °C for NC-Clay, whereas for clay, a two-step reduction with the initial step reduction at around 560 °C and the second step at 610 °C can be seen. The peak at 228 °C can be ascribed to overlapping easily reducible Co oxide and Ni oxide via NiO → Ni^{X+} and Co_3O_4 → Co^{Y+} and reducing adsorbed oxygen. Fig. 5d shows the deconvolution of the main species to give relative information of the different species present that can be reduced. The main uptake occurring at a lower temperature for NC-Clay might indicate the surface reduction of Co oxide to cobalt. It can also be observed that the NC-Clay catalyst, when compared to the pristine clay catalyst, gets drastically reduced at a lower initial reduction temperature of around 262 °C, which is an indication of the NC-Clay catalytic system promoting a good redox property. The highest peak at 262 °C can be attributed to the reduction of Ni^{X+} → Ni metal and Co^{Y+} → Co metal.[45,46] Moreover, it reveals that the surface has many oxygen species that are highly mobile with rapid active site regeneration for H_2 adsorption.[44] The amount of H_2 uptake of

the synthesized NC-Clay catalyst indicated an increase with 3987 μmol g⁻¹ compared to the 895 μmol g⁻¹ for pristine clay, which might be a result of the incorporation of Ni and Co. In comparison, the bare clay was characterized by the presence of a broad peak with maxima at temperatures of 553 °C and 795 °C. The observed increased reduction at lower temperatures can be ascribed to the weakened clay bond due to the introduction of Ni and Co, which promoted the metal–clay interaction, in turn, increasing the lattice oxygen mobility in the NC-Clay catalyst. The peak at 470 °C for the NC-Clay catalyst can be attributed to the bulk NiO peak, which is loosely bonded to the clay species. The broad shoulder peaks at higher temperatures starting from 610 °C might indicate uniformly dispersed particles, as can be confirmed from the TEM mapping image (Fig. S3, ESI†). The details are given in Table 1. It can be observed from Fig. 5e that both Ni Clay and Co Clay samples show reducibility at a higher temperature compared to NC-Clay samples. For Co clay, two broad shoulder peaks were observed at 354 °C and 425 °C. However, Ni clay showed initial reducibility with a broad peak starting at around 375 °C, followed by a weakened peak at 532 °C and a broader peak around 607 °C. It is evident that with the introduction of Ni and Co metal into the clay, there is an increase in reducibility as the oxides of these metals are easily reducible under H_2. The use of both the species significantly promotes higher reducibility in the NC-Clay catalyst as compared to when used separately. Hence, it can be inferred that the bimetal (Ni and Co) incorporation in clay makes a better catalyst (as can be seen from the soot oxidation data). The low temperature might be due to the presence of easily reducible oxides of Ni and Co.[43] Additionally, there is an observed increase in the intensity of the peak, which amounts to increased H_2 consumption. The NC-Clay catalyst after deconvolution exhibited the largest peak area at 262 °C with maximum oxygen storage capacity (OSC), which is an essential parameter in the

catalytic application for storing and releasing active oxygen species. As a result, the synthesized NC-Clay is promising for use as a catalyst in soot oxidation.

TGA is a general method for characterizing the soot oxidation activity of a catalyst where the catalyst is subjected to model soot, generally carbon black. A schematic is shown in Fig. 6a. The measurement was performed at a heating rate of 10 °C min⁻¹ on an STA (Simultaneous Thermal Analyser) in a temperature range of 30 °C to 900 °C in a gas flow (zero air) of 20 mL min⁻¹. For analysis of the catalyst prepared, soot (obtained from Printex U) was mixed with the catalyst in a 1 : 4 ratio in tight contact mode by grinding in a mortar pestle for 15 min. The average temperature reported in the literature ranges from 400 to 500 °C for a good soot oxidation catalyst. Additionally, the bare carbon without any catalyst showed a high T_{50} of nearly 745 °C (as shown in the ESI,† Fig. S4). We are reporting a Ni–Co co-doped clay catalyst as a novel material for soot oxidation with the T_{50} temperature reduced to 358 °C, as shown in Fig. 6b. It can also be observed that Ni-Clay and Co-Clay individually and also when used in an equal amount of weight % do not significantly reduce the temperature as observed from Fig. 6b. The increase in the activity of the prepared clay catalyst can be due to the presence of labile lattice oxygen indicated by the XPS study and the improved mobility of the more oxygen species present, as noted in the O_2 TPD study. The easy and strong desorption indicated the generation of active oxygen accelerating the soot oxidation reaction. The incorporation of both Ni and Co in clay showed a synergistic effect, aiding the catalytic activity inducing mobility and transfer of active species from the bulk to the surface.

To further investigate the chemical kinetics happening during the oxidation of soot in the presence of the synthesized catalyst, experiments were carried out at different heating rates of 7, 5, 3 and 1° min⁻¹ for the synthesized NC-Clay catalyst as
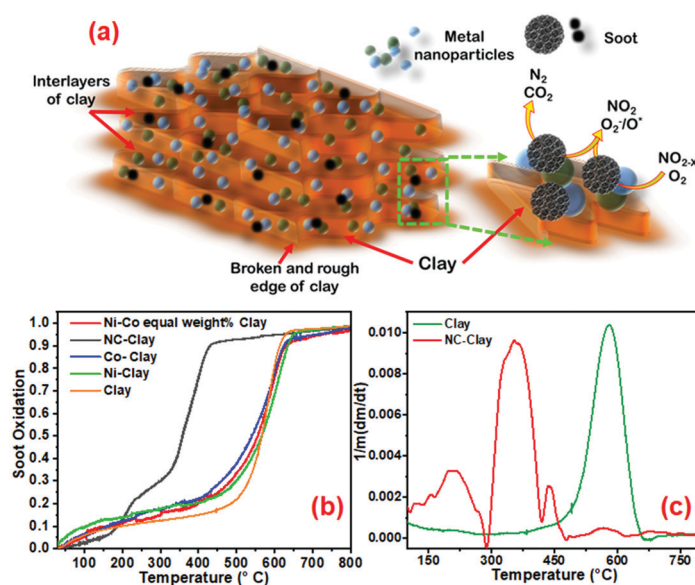

Fig. 6 (a) Schematic representation of soot oxidation of the NC-Clay catalyst, (b) soot oxidation activity of NC-Clay, and (c) differential mass plot showing oxidation at a different area.
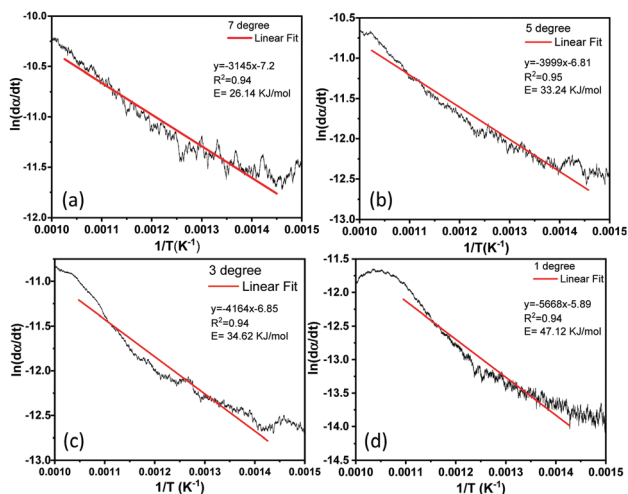
Fig. 7 Activation energy (reported in kJ mol⁻¹) calculation using the Friedman method, (a)–(d) at different heating rates of 7, 5. 3 and 1 °C min⁻¹ of the NC-Clay catalyst.

shown in Fig. 7a–d respectively. The reactivity of the soot is calculated *via* the Friedman method[47] whereby according to eqn (1), the activation energy, E/R can be obtained from the plot of $\ln(d\alpha/dt)$ *vs.* $1/T$, where A, E and $f(\alpha)$ are respectively the pre-exponential factor, the activation energy and the reaction model.[48,49]

$$\ln\left(\mathrm{HR}\left(\frac{d\alpha}{dT}\right)\right) = \ln A + \ln f(\alpha) - E/RT \qquad (1)$$

The Friedman method is among the many model-free methods available to apply to various data sets at varying heating rates.[50–52] The various activation energies of the synthesized NC-Clay catalyst are indicated in Fig. 7. Additionally, following a similar strategy, soot without any catalyst support has also been subjected to various degrees of heating rate and it was found that in comparison with the NC-Clay supported soot oxidation it had lower activation energy. Furthermore, the activation energy of various synthesized catalysts such as Clay, Ni-Clay, Co-Clay and Ni and Co-doped Clay at equal amounts has been evaluated (Fig. S6 in the ESI†). It was observed that NC-Clay compared to these various materials had the lowest activation energy. This can be attributed to the increase in active oxygen species due to the simultaneous incorporation of both Ni and Co in the layered clay material. This is in accordance with the observed trend in the XPS study and both O_2 TPD and H_2 TPR studies in Fig. 4 and 5.

Therefore, it can be inferred that the improved reducibility (as observed from the H_2 TPD study, Table 1) indicated an enhanced capacity to release lattice oxygen that participates in the reaction. The soot oxidation activity of the prepared catalyst is indicated in Fig. 6c as a 1st order derivative with different zones of oxidation. The highest peak for the NC-Clay catalyst showed a drastic improvement compared to the pristine clay catalyst at 578 °C, thus deducing that inert clay can serve as a suitable catalyst with appropriate incorporation of a metal catalyst. The good catalytic activity achieved in this study can be attributed to an increase in surface adsorbed oxygen and improved redox property in the NC-Clay catalyst, which agrees well with the chemical analysis data presented above. Furthermore, the catalyst has been tested for up to 5 cyclability tests with a modest loss of activity (Fig. S5, ESI†). Additionally, the spent catalyst was analysed using XPS, XRD and TEM (Fig. S7, ESI†) to observe any changes in the chemical nature, structural and morphological environment after being used as a catalyst in the soot oxidation experiment. It can be deduced that the catalyst showed minimum changes after the soot oxidation process.

Conclusions

Natural clay was modified using Ni and Co NPs, wherein the clay acted as a support material for the metal NPs to interact with the soot material for improved soot oxidation activity. The introduction of bi-metals brought in noticeable changes in the physical, chemical, and catalytic properties of the catalyst, which can be considered as a result of the synergistic effect of both the metals. The H_2-TPR results suggest a good redox property. Moreover, active sites and surface oxygen with labile species help achieve soot oxidation at a T_{50} temperature as low as 358 °C. This is the first study where bi-metal incorporation of Co and Ni has been carried out in clay for soot oxidation. The current study creates new possibilities to design catalytic converters that are of low cost and sustainable with high efficiency.

Conflicts of interest

The authors declare no conflicts of interest.

Acknowledgements

References

1 World Health Organization (WHO), WHO Releases Country Estimates on Air Pollution Exposure and Health Impact, http://www.who.int/mediacentre/news/releases/2016/air-pollution-estimates/en/, accessed 1 October, 2019.
2 Oxford, https://www.lexico.com/en/definition/soot, accessed 10 October, 2019.
3 J. Weidman and S. Marshall, Soot Pollution 101, What You Need to Know and How You Can Help Prevent It, accessed 10 October, 2019.

4 K. Balakrishnan, S. Ghosh, G. Thangavel, S. Sambandam, K. Mukhopadhyay, N. Puttaswamy, A. Sadasivam, P. Ramaswamy, P. Johnson, R. Kuppuswamy, D. Natesan, U. Maheshwari, A. Natarajan, G. Rajendran, R. Ramasami, S. Madhav, S. Manivannan, S. Nargunanadan, S. Natarajan, S. Saidam, S. Chakraborty, L. Balakrishnan and V. Thanasekaraan, *Environ. Res.*, 2018, **161**, 524–531.

5 D. Jampaiah, V. K. Velisoju, D. Devaiah, M. Singh, E. L. H. Mayes, V. E. Coyle, B. M. Reddy, V. Bansal and S. K. Bhargava, *Appl. Surf. Sci.*, 2019, **473**, 209–221.

6 D. Laishram, K. P. Shejale, R. Gupta and R. K. Sharma, *ACS Sustainable Chem. Eng.*, 2018, **6**, 11286–11294.

7 E. Aneggi, J. Llorca, A. Trovarelli, M. Aouine and P. Vernoux, *Chem. Commun.*, 2019, **55**, 3876–3878.

8 Y. Gao, X. Wu, S. Liu, D. Weng and R. Ran, *Catal. Surv. Asia*, 2018, **22**, 230–240.

9 J. C. Martínez-Munuera, M. Zoccoli, J. Giménez-Mañogil and A. García-García, *Appl. Catal., B*, 2019, **245**, 706–720.

10 Q. N. Tran, F. Martinovic, M. Ceretti, S. Esposito, B. Bonelli, W. Paulus, F. Di Renzo, F. A. Deorsola, S. Bensaid and R. Pirone, *Appl. Catal., A*, 2020, **589**, 117304.

11 C. M. Álvarez-Docio, R. Portela, J. J. Reinosa, F. Rubio-Marcos, C. Granados-Miralles, L. Pascual and J. F. Fernández, *Appl. Catal., A*, 2020, **591**, 117404.

12 A. Rangaswamy, P. Sudarsanam and B. M. Reddy, *J. Rare Earths*, 2015, **33**, 1162–1169.

13 P. Sudarsanam, B. Hillary, M. H. Amin, N. Rockstroh, U. Bentrup, A. Brückner and S. K. Bhargava, *Langmuir*, 2018, **34**, 2663–2673.

14 P. Sudarsanam, B. Hillary, B. Mallesham, B. G. Rao, M. H. Amin, A. Nafady, A. M. Alsalme, B. M. Reddy and S. K. Bhargava, *Langmuir*, 2016, **32**, 2208–2215.

15 M. V. Grabchenko, G. V. Mamontov, V. I. Zaikovskii, V. La Parola, L. F. Liotta and O. V. Vodyankina, *Appl. Catal., B*, 2020, **260**, 118148.

16 G. Si, J. Yu, X. Xiao, X. Guo, H. Huang, D. Mao and G. Lu, *Mol. Catal.*, 2018, **444**, 1–9.

17 F. Morfin, T.-S. Nguyen, J.-L. Rousset and L. Piccolo, *Appl. Catal., B*, 2016, **197**, 2–13.

18 A. Satsuma, M. Yanagihara, J. Ohyama and K. Shimizu, *Catal. Today*, 2013, **201**, 62–67.

19 A. Gayen, K. R. Priolkar, P. R. Sarode, V. Jayaram, M. S. Hegde, G. N. Subbanna and S. Emura, *Chem. Mater.*, 2004, **16**, 2317–2328.

20 K. Krishna, A. Bueno-López, M. Makkee and J. A. Moulijn, *Appl. Catal., B*, 2007, **75**, 189–200.

21 K.-i. Shimizu, H. Kawachi and A. Satsuma, *Appl. Catal., B*, 2010, **96**, 169–175.

22 H. Zhao, X. Zhou, M. Wang, Z. Xie, H. Chen and J. Shi, *RSC Adv.*, 2017, **7**, 3233–3239.

23 Y.-C. Tsai, N. N. Huy, D. C. W. Tsang and K.-Y. A. Lin, *J. Colloid Interface Sci.*, 2020, **561**, 83–92.

24 C. M. Álvarez-Docio, R. Portela, J. J. Reinosa, F. Rubio-Marcos, L. Pascual and J. F. Fernández, *Catalysts*, 2020, **10**, 406.

25 M. Zhao, J. Deng, J. Liu, Y. Li, J. Liu, Z. Duan, J. Xiong, Z. Zhao, Y. Wei, W. Song and Y. Sun, *ACS Catal.*, 2019, **9**, 7548–7567.

26 A. A. Voskanyan and K. Y. Chan, *ACS Appl. Nano Mater.*, 2018, **1**, 556–563.

27 V. K. Soni, P. R. Sharma, G. Choudhary, S. Pandey and R. K. Sharma, *ACS Sustainable Chem. Eng.*, 2017, **5**, 5351–5359.

28 V. K. Soni and R. K. Sharma, *ChemCatChem*, 2016, **8**, 1763–1768.

29 C. H. Zhou, *Appl. Clay Sci.*, 2011, **53**, 87–96.

30 B.-L. Zhu, C.-L. Qi, Y.-H. Zhang, T. Bisson, Z. Xu, Y.-J. Fan and Z.-X. Sun, *Appl. Clay Sci.*, 2019, **179**, 105138.

31 B. Tyagi, C. D. Chudasama and R. V. Jasra, *Spectrochim. Acta, Part A*, 2006, **64**, 273–278.

32 P. Shi, X. Dai, H. Zheng, D. Li, W. Yao and C. Hu, *Chem. Eng. J.*, 2014, **240**, 264–270.

33 Z. Chen, C. X. Kronawitter and B. E. Koel, *Phys. Chem. Chem. Phys.*, 2015, **17**, 29387–29393.

34 X. Liang, Z. Ren, X. Zhu, Q. Zhang, D. Mei and B. Chen, *J. Phys. Chem. C*, 2017, **121**, 24588–24593.

35 S. Dutta, A. Indra, Y. Feng, T. Song and U. Paik, *ACS Appl. Mater. Interfaces*, 2017, **9**, 33766–33774.

36 M. Zhou, Q. Weng, X. Zhang, X. Wang, Y. Xue, X. Zeng, Y. Bando and D. Golberg, *J. Mater. Chem. A*, 2017, **5**, 4335–4342.

37 J.-C. Dupin, D. Gonbeau, P. Vinatier and A. Levasseur, *Phys. Chem. Chem. Phys.*, 2000, **2**, 1319–1324.

38 E. E. Miró, F. Ravelli, M. A. Ulla, L. M. Cornaglia and C. A. Querini, *Catal. Today*, 1999, **53**, 631–638.

39 M. Iwamoto, Y. Yoda, N. Yamazoe and T. Seiyama, *J. Phys. Chem.*, 1978, **82**, 2564–2570.

40 L. Nossova, G. Caravaggio, M. Couillard and S. Ntais, *Appl. Catal., B*, 2018, **225**, 538–549.

41 C. Bouly, K. Chandes, D. Maret and D. Bianchi, in *Studies in Surface Science and Catalysis*, ed. A. Frennet and J. M. Bastin, Elsevier, 1995, vol. 96, pp. 261–274.

42 D. Mukherjee, D. Devaiah, P. Venkataswamy, T. Vinodkumar, P. G. Smirniotis and B. M. Reddy, *New J. Chem.*, 2018, **42**, 14149–14156.

43 M. Muñoz, S. Moreno and R. Molina, *Int. J. Hydrogen Energy*, 2014, **39**, 10074–10089.

44 X. Lin, S. Li, H. He, Z. Wu, J. Wu, L. Chen, D. Ye and M. Fu, *Appl. Catal., B*, 2018, **223**, 91–102.

45 H. Ay and D. Üner, *Appl. Catal., B*, 2015, **179**, 128–138.

46 V. Palma, C. Ruocco, E. Meloni and A. Ricca, *Catalysts*, 2017, **7**(8), 226.

47 H. L. Friedman, *J. Polym. Sci., Part C: Polym. Symp.*, 1964, **6**, 183–195.

48 P. P. Morajkar, M. K. Abdrabou, A. V. Salkar, A. Raj, M. Elkadi and D. H. Anjum, *Energy Fuels*, 2020, **34**, 12960–12971.

49 P. P. Morajkar, M. K. Abdrabou, A. Raj, M. Elkadi, S. Stephen and M. Ibrahim Ali, *Fuel*, 2020, **280**, 118631.

50 E. Biagini, L. Guerrini and C. Nicolella, *Energy Fuels*, 2009, **23**, 3300–3306.

51 P. P. Morajkar, G. D. J. Guerrero Peña, A. Raj, M. Elkadi, R. K. Rahman, A. V. Salkar, A. Pillay, T. Anjana and M. S. Cha, *Energy Fuels*, 2019, **33**, 12852–12864.

52 M. K. Abdrabou, P. P. Morajkar, G. D. J. Guerrero Peña, A. Raj, M. Elkadi and A. V. Salkar, *Fuel*, 2020, **275**, 117918.